

## Flow structure and turbulence in the near field of an immiscible buoyant oil jet

Xinzhi Xue , Lakshmana Dora Chandrala , and Joseph Katz \*

*Department of Mechanical Engineering, Johns Hopkins University, Baltimore, Maryland 21218, USA*



(Received 20 August 2020; accepted 22 December 2020;  
published 2 February 2021)

This experimental study investigates the evolution of mean flow and turbulence in the near field of an immiscible buoyant oil jet injected into water at a low Reynolds number ( $Re = 1230$ ). Refractive index matching of the liquid pair using silicone oil and sugar water enables simultaneous applications of particle image velocimetry and planar laser induced fluorescence. The results include flow visualizations, ensemble-averaged phase and velocity distributions, and Reynolds normal and shear stresses for each phase and combined. Trends are compared to those of a single-phase jet. Close to the nozzle, the surrounding water gains momentum when thin layers are entrained into the jet. Also, as oil ligaments begin to extend outward, water-containing vortices form around their tips. Further downstream, as the oil breaks up into blobs and then to smaller droplets, the spreading rate of the oil volume fraction and the decrease in its centerline concentration are lower than those of the axial momentum and centerline velocity. Universal profiles of either the phase distribution or the axial momentum scaled with the half widths and centerline values develop after six diameters, the latter occurring earlier than the single-phase jet. As expected, the mean velocity in the oil is higher than that in the water, and after thirteen diameters, the difference between them is consistent with the buoyant rise velocity of oil droplets with the same Sauter mean diameter in turbulent flows. Initially, the normal and shear Reynolds stress components in the oil jet are higher than those in the single-phase jet, but the differences between them decrease with axial distance. Phase-conditioned statistics in the oil jet reveal significant spatially varying discrepancies between the turbulence level in the oil and water phases. The peripheral turbulence in the water is higher near the jet exit, but lower after six diameters. The latter trend is attributed to the intermittency and lower peripheral shear-dominated turbulence production rate in the entrained water. In contrast, near the jet centerline, the turbulence production rate, hence the turbulent kinetic energy, is higher in the water. Here, while the axial contraction increases the turbulence in both phases, the radial extension in the spreading oil, as opposed to the radial contraction in the entrained water, causes a discrepancy in the production rates. After thirteen diameters, the differences between oil and water turbulence levels diminish. Still, the axial velocity fluctuations are substantially higher than the radial ones. The oil blob size distribution in this region still has a Sauter mean diameter that is five times larger than that measured after thirty diameters, indicating that fragmentation of the oil persists well beyond the range examined in this paper.

DOI: [10.1103/PhysRevFluids.6.024301](https://doi.org/10.1103/PhysRevFluids.6.024301)

---

\*Corresponding author: [katz@jhu.edu](mailto:katz@jhu.edu)

## I. INTRODUCTION

Immiscible multiphase buoyant jets and plumes, which consist of a momentum and buoyancy-driven dispersed phase (bubbles, droplets, or particles) discharged into a quiescent or coflowing continuous phase, are important in a variety of engineering, geophysical, and environmental processes. Some examples include spray atomization [1], volcanic eruption [2], and subsurface oil spill [3–7]. These multiphase jets and plumes have some different features than the miscible or single-phase jets and plumes [8–14]. For miscible single-phase flow, the discharged fluid is irreversibly mixed at scales on which molecular diffusivity dominates (the Batchelor scale). Instead, multiphase jets and plumes fragment near the discharge exit and contain distinct interfaces between two phases at scales that vary with the droplet size distributions. While there is little to no scalar mixing and density changes within each phase, the soluble components and momentum can still diffuse across the interfaces due to stresses, along with buoyancy- and interfacial tension-related instabilities [15–17].

Flows containing very small volume fractions ( $\gamma \ll 1$ ) of small particles satisfying  $D < \eta$ , where  $D$  is the particle size and  $\eta$  is the Kolmogorov scale, have a continuous phase turbulence that is nearly the same as that of the single-phase counterparts [18]. However, at high volume fraction, or  $D > \eta$ , as typically occurs in the near field of an immiscible liquid jet, the presence of a dispersed phase could either cause turbulence attenuation or enhancement [19–21]. The transfer of momentum and energy between phases in suspension laden flows can be affected by the shape, deformation of the dispersed phase, and the relative motions between the two phases [22–24]. It is essential to understand and predict how the turbulence is generated and modulated by the addition of length and timescales associated with the immiscible interfaces. Such data would be beneficial for extending the classical theories for the mean velocity, Reynolds stresses, and self-similarity assumptions in jets and plumes [25,26] to more generalized non-Boussinesq multiphase models [27–30].

The difficulties to simulate turbulent multiphase flows owing to the wide range of scales involved, and the challenges in measuring them, are summarized in Ref. [31]. Yet, recent progress has led to a better understanding of the fragmentation, entrainment, and the evolution of droplet size distributions in liquid-liquid immiscible jets and plumes [32–34]. A comprehensive summary is provided in Ref. [35]. Considerable knowledge has also been generated about the physical processes affecting the fragmentation of liquid jets in the air [36–40]. Conversely, there are very limited experimental data on the flow structure and turbulence in the near field of immiscible buoyant liquid jets in another liquid, such as oil jets in water, where phase interactions, fragmentation, and droplet formation play dominant roles.

This experimental study focuses on the near field flow structures, ensemble-averaged phase distributions, Reynolds stresses, and turbulence production rate of each phase in the fragmentation region of a vertical buoyant jet. A refractive index-matched immiscible fluids pair, and simultaneous particle image velocimetry (PIV) and planar laser-induced fluorescence (PLIF) are used for probing this flow. The present statistical analysis follows an earlier paper [41], where the same fluids have been used for demonstrating the prevalent formation of compound droplets and their size distributions. Details of the experimental setup and procedures are presented in Sec. II. Next, Sec. III describes the streamwise evolution of the mean velocity profiles, root mean square (rms) values of velocity fluctuations, and Reynolds shear stress. The differences between the evolution of the oil volume fraction and mean momentum distribution are also presented. Trends are compared with those of a single-phase jet at a very similar Reynolds number. Among the findings, the phase-conditioned turbulence statistics reveal a sizable difference between the mean velocity, turbulence level, and the Reynolds shear stress in the two phases along the periphery of the jet. It is demonstrated that the difference in peripheral turbulence can be linked to the intermittency of the water flow. Furthermore, partitioning of the terms contributing to the turbulence production indicates that shear production is the dominant term along the periphery of the jet, and that there is a significantly higher total production rate in the water near the centerline of the jet. Finally, the conclusions are presented in Sec. IV.

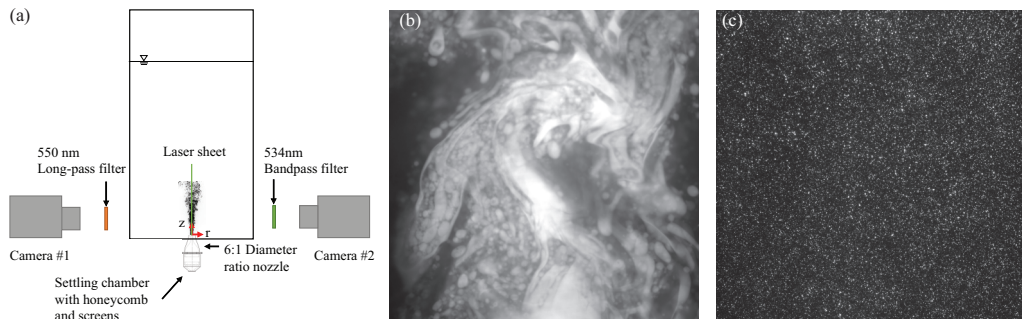


FIG. 1. (a) The experimental setup for simultaneous PLIF and PIV measurements; (b) sample raw PLIF image from camera 1, and (c) sample raw PIV image from camera 2. Both images are located at  $z/d = 5.7-7.8$ .

## II. FACILITY AND EXPERIMENTAL METHODS

Aiming to understand processes relevant to fragmentation of oil jets in seawater, the present study utilizes two immiscible refractive index-matched fluids that have the relevant interfacial tension, viscosity, and density ratios. The selected liquid pair consists of silicone oil (polydimethylsiloxane, trimethylsiloxy terminated) as the injected liquid, and sugar water (64% by weight) as the surrounding phase. The density  $\rho_o$  and the viscosity  $\mu_o$  of the dispersed silicone oil are  $960 \text{ kg/m}^3$  and  $(2.40 \pm 0.2) \times 10^{-2} \text{ kg/m s}$ , respectively, and those ( $\rho_w$  and  $\mu_w$ ) of the ambient sugar water are  $1155 \text{ kg/m}^3$ , and  $(5.65 \pm 0.2) \times 10^{-3} \text{ kg/m s}$ , respectively. Their interfacial tension  $\sigma$  is  $(27 \pm 0.5) \times 10^{-3} \text{ N/m}$ . These properties have been measured in our laboratory using procedures described in [41,42]. To observe the oil, it is mixed with a fluorescent dye (Nile Red). As shown in Fig. 1(a), the experiments have been performed in a  $39 \times 24.1 \times 76.2 \text{ cm}^3$  acrylic tank filled with sugar water. The silicone oil is injected from a regulated nitrogen-pressurized reservoir through a flowmeter (Omega, FL-6110A), a settling chamber containing honeycomb and screens, and a nozzle with a 6.35:1 diameter ratio. The exit nozzle diameter  $d$  of the initially laminar jet is 10 mm. In a separate set of experiments aimed at establishing a baseline, sugar water is injected using the same setup, except for the flowmeter (Omega, FL-6320ABR). The two experiments are performed at nearly the same Reynolds number. Based on the PIV measurements (described below), the centerline velocities of the oil and sugar-water jet close to the nozzle exit are  $U_0 = 4.2$  and  $0.8 \text{ m/s}$ , respectively. The corresponding mean exit velocities are  $U_{\text{mean}} = 3.1$  and  $0.57 \text{ m/s}$ . These values are calculated by integrating the mean velocity profiles close to the exit from the nozzle. The typical magnitudes of the backflow velocity along the periphery of the jet, at a point located at  $z/d = 2$ , are  $2.6 \times 10^{-3}$  and  $4.8 \times 10^{-4} \text{ m/s}$ , for the oil and single-phase jets, respectively. Being about 0.1% of the exit velocity, this flow is not expected to have a significant impact on the near field dynamics of the jet. The relevant nondimensional numbers are defined as (i) the jet Reynolds number,  $\text{Re} = \rho_o U_{\text{mean}} d / \mu_o$ ; (ii) the Ohnesorge number,  $\text{Oh} = \mu_o / \sqrt{\rho_o \sigma d}$ ; and (iii) the combined density and viscosity ratio,  $\Gamma = \mu_o \rho_w^{1/2} / \mu_w \rho_o^{1/2}$ . The jet Reynolds number are  $\text{Re} = 1230$  and  $1170$  for the oil and single-phase water jet, respectively. The Ohnesorge number and the combined density and viscosity ratio for the oil jet are  $\text{Oh} = 0.047$ , and  $\Gamma = 5.61$ . Based on these  $\text{Re}$  and  $\text{Oh}$ , the oil jet falls into the liquid-liquid atomization regime [43].

The oil jet structure presented is measured using simultaneous PIV and PLIF in three downstream regions:  $z/d = 0.1-2.1$ ,  $5.7-7.8$ , and  $11.8-13.8$ , where  $z$  is the axial location, with  $z = 0$  located at the center of the nozzle. We opted to focus on the very near field of the jet since most of the fragmentation and droplet generation occurs in this region, as our previous observations have shown [41]. The Morton length,  $l_M = M_s^{3/4} / B_s^{1/2}$ , where  $M_s$  is the source momentum flux, and  $B_s$  is the source buoyancy flux [44,45], is  $0.225 \text{ m}$  ( $z/d = 22.5$ ). Therefore, for the present measurement range, the jet falls into the momentum-driven regime. The center plane of the jet is illuminated by

a sheet of pulsed 532-nm Nd:YAG laser with a thickness of about 1 mm. The synchronized PIV and PLIF images are recorded with two identical cameras (PCO.dimax) located on opposite sides of the light sheet. The fluid is seeded with silver-coated glass particles that have a density  $\rho_p = 3091 \text{ kg/m}^3$ , and mean particle diameter  $d_p = 2 \text{ }\mu\text{m}$ . Using the streamwise velocity fluctuations  $u'$ , and assuming characteristic eddies of the same order as the exit nozzle diameter  $d$ , the Stokes number of the seed particles, representing the particle response time relative to that of the flow, can be estimated from  $St = \rho_p d_p^2 U_0 / 18 \mu_w d$  [46]. The results,  $2.1 \times 10^{-6}$  for the oil, and  $9.0 \times 10^{-6}$  for the water, indicate that the particles can track the flow accurately. The settling velocity of such particles in the quiescent flow region is  $0.8 \text{ }\mu\text{m/s}$ ; therefore the effects on the measurements in this region are negligible. While the PIV particles reflect the laser light at the illumination wavelength, the silicone oil fluoresces at a peak wavelength of 650 nm. To separate the signals, a 534-nm fluorescence bandpass filter with a 25-nm bandwidth is placed in front of the PIV camera lens to reject the fluorescence signal, and a long-pass filter with a cutoff wavelength of 550 nm is placed in front of the PLIF camera to remove the reflected 532-nm laser light. A sample pair of raw PLIF and PIV images is shown in Figs. 1(b) and 1(c), respectively. Both the PIV and PLIF images ( $2016 \times 2016 \text{ pixel}^2$ ) are recorded at 15 image pairs per second with  $50 \text{ }\mu\text{s}$  interframe time. The PLIF images, which have a resolution of  $11.4 \text{ }\mu\text{m/pixel}$ , are positioned to cover the entire PIV field of view whose resolution is  $10.7 \text{ }\mu\text{m/pixel}$ . Each run lasts only a few seconds before some of the oil circulates back to the vicinity of the nozzle exit, allowing the acquisition of approximately 100 image pairs during the steady-state phase of this run. A total of 2500 realizations are recorded at each location and for each jet to obtain the flow and turbulence statistics of the jet.

For the PIV measurements, the images are enhanced, as described in Ref. [47], and the velocity is calculated by cross correlations using the LAVISION DAVIS software. The PIV image pairs are processed using a multipass, iterative window deformation scheme with an initial window size of  $64 \times 64$  pixels and 50% overlap for the first two passes, and  $24 \times 24$  pixels window size with 50% overlap for the next two passes. After each pass, results are evaluated using a universal outlier detection scheme [48] and bad vectors are replaced by the median value of the surrounding vectors. The final vector spacing is  $128.5 \text{ }\mu\text{m}$ . Calculations of the correlation coefficient between successive instantaneous velocity vectors have confirmed that the samples are statistically independent. The relative uncertainty of PIV measurements varies spatially increasing with decreasing velocity. The characteristic particle displacements vary from 20 pixels at the jet centerline to 5 pixels in the outer part of the shear layer along the periphery of the jet. The characteristic uncertainty in displacement for cross correlation based velocity measurements is on the order of 0.1 pixel [49] as long as the window contains about ten particles, the signal to noise ratio is high, and the particle image size is large enough not to be affected by peak locking. Hence, the estimated relative uncertainty in the local velocity for most of the present jet varies between 0.5% and 2%. To assess the magnitude and impact of the backflow surrounding the jet, we also cross correlate images recorded 66 ms apart. For the segmentation of the oil and water phase from the PLIF data, a random forest based pixelwise classification is applied, the details of which are provided in a previous paper [41]. Spatial matching between the PIV and PLIF images is performed by placing a transparent dotted grid at the jet centerline and recording its image by both cameras. An affine geometric transformation and bicubic interpolation are used for precise image registration of corresponding images. For the experiments aimed to obtain baseline single-phase data of a sugar-water jet injected into sugar water, the PIV image pairs have been recorded at 1 Hz with  $300 \text{ }\mu\text{s}$  interpair delay using a  $6600 \times 4400 \text{ pixel}^2$  camera. In this case, the total number of realizations is 1000, and the resolution of the PIV images is  $14.8 \text{ }\mu\text{m/pixel}$ , which corresponds to a vector spacing of  $177.6 \text{ }\mu\text{m}$ .

### III. RESULTS

#### A. Flow structures and mean flow characteristics

To characterize the near field evolution of the buoyant oil jet structures, we first examine the flow and oil-water interfaces at three different streamwise locations. Samples of contour maps of instantaneous velocity magnitude are presented separately for the oil and water phases in Fig. 2. Note that for convenience, different signs of  $r$  are used to denote opposite sides of the jet. The left column focuses on the oil, and the right column, on the water. At  $z/d = 0.1-2.1$  [Figs. 2(a) and 2(b)], the interface becomes wavy due to the Kelvin-Helmholtz (KH) instability, with most of the momentum concentrated in the oil. Most of the ambient flow has a very low velocity, except for the regions where the water ligaments begin to penetrate into the oil, and oil ligaments start to extend outward. There, the water velocity increases rapidly, reaching about 60% of the  $U_0$ . A closer look at another sample is presented in Figs. 3(a) and 3(b), which focuses on the early KH rollup along with the oil-water interface. Even before entrainment, the vorticity is already extended to both phases, and once the ligaments form, the water momentum increases rapidly. The vortices forming in the water appear to be centered around the tips of the oil ligaments, e.g., at  $r/d = -0.58$  and  $z/d = 1.14$ . Interestingly, in these regions, the vorticity is mostly concentrated in the water, while the oil ligaments mostly have low vorticity. Further insight into the role of vortical structures can be gained by examining the distribution of swirling strength, defined as the magnitude of the imaginary part of complex eigenvalues of the velocity gradient tensor [50], Fig. 3(c), shows the distribution of the two-dimensional version of this parameter,  $\lambda_{2D}$ , as introduced in Ref. [51]. It confirms that the center of vortical structures either coincides with or is located in the vicinity of the tip of the oil ligament or the base of entrained water ligaments.

Further downstream, at  $z/d = 5.7-7.8$  [Figs. 2(c) and 2(d)], the oil is partially fragmented and meanders, but still maintains a high momentum core containing mostly oil. Water with high velocity already appears between the fragmenting oil blobs. The periphery contains both oil and water ligaments with low momentum and sizes comparable to the jet diameter. Some of the oil blobs can still be seen at  $z/d = 11.8-13.8$ , but most of them have already broken into separate droplets, with many appearing to be compound droplets, consistent with the observations reported in Ref. [41]. A meandering region with elevated momentum is still evident, but it contains a mixture of both phases. Outside of it, the velocity of both phases is low with magnitudes falling in the  $0.2-0.3 U_0$  range.

To characterize the ensemble-averaged near field, we first quantify the axial development of two jet spreading indicators: (i) the velocity half width,  $b_{1/2}$ , defined as the radial location where the mean velocity decreases to half of its local centerline values, and (ii) the jet oil fraction half width,  $b_{\gamma 1/2}$ , where the oil volume fraction decreases to half of its local centerline value. Figure 4(a) shows the streamwise evolution of  $b_{1/2}$  and  $b_{\gamma 1/2}$  for the oil jet and compares that to  $b_{1/2}$  of the single-phase jet at nearly the same Reynolds number. Figure 4(b) presents the corresponding values of the centerline velocity,  $U_{cl}$ . For the single-phase baseline case, near the nozzle, the half width remains nearly constant up to  $z/d = 7$ . Accordingly, the centerline mean velocity remains very close to that at the nozzle exit, with only a slight (3%) decay by  $z/d = 7$ . At  $z/d > 8$ ,  $b_{1/2}$  increases almost linearly with  $z/d$ . The spreading rate,  $S = \partial b_{1/2} / \partial z$ , is equal to 0.11, consistent, e.g., with a prior study of single-phase jet ( $S = 0.113$ ) at a moderate but higher Reynolds number,  $Re = 2679$  [52]. The decay of the centerline velocity is typically defined as  $U_0/U_{cl}(z) = C(z - z_0)/d$ , where  $C$  is the decay rate and  $z_0$  is the virtual origin [9]. Fitting to the current data gives  $C = 0.24$  and  $z_0 = 3.4d$ , consistent with a prior study at a similar Reynolds number ( $Re = 1350$ ) by the authors of Ref. [53], where  $C = 0.24$ , and  $z_0 = 3.0d$ . In Ref. [52],  $C = 0.17$ .

For the oil jet,  $b_{1/2}$  and the centerline velocity remain unchanged at  $z/d = 0.1-2.1$ . By  $z/d = 5.8$ , the jet is already expanding, and the streamwise velocity is decreasing, both earlier than that of the single-phase jet. Yet, once it starts, the spreading rate of the oil jet,  $S = 0.10$ , is quite similar to that of the single-phase case all the way up to  $z/d = 13.8$ . Accordingly, the centerline velocity of the oil jet starts to decrease along the axial direction with the same decay rate  $C = 0.24$  of the

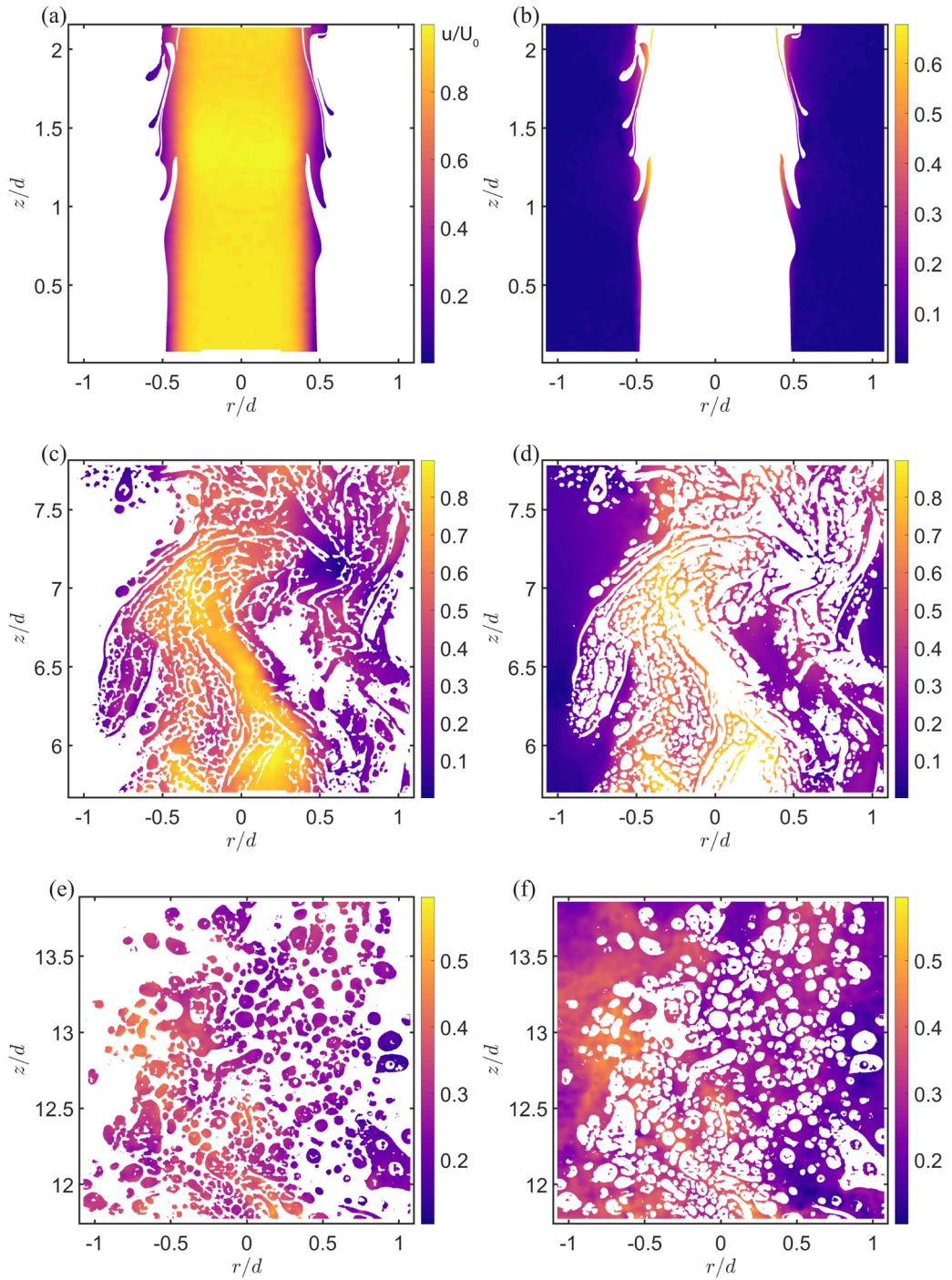


FIG. 2. Samples of instantaneous velocity magnitude  $u$  normalized by the jet mean centerline exit velocity,  $U_0 = 4.2$  m/s, at  $z/d = 0.1-2.1$ ,  $5.7-7.8$ , and  $11.8-13.8$ . (a), (c), (e) oil phase, and (b), (d), (f) water phase.

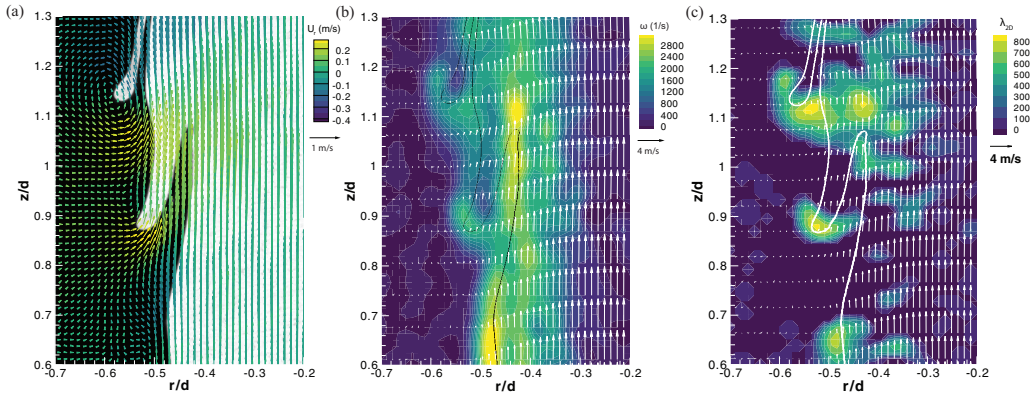


FIG. 3. A sample of magnified instantaneous flow field of an (a) oil jet in water overlaid with the oil-water interface, (b) the same oil jet in water overlaid with vorticity magnitude, and (c) the same oil jet in water overlaid with swirling strength. Vectors in (b), (c) are diluted by 4 in the axial direction and rescaled for clarity.

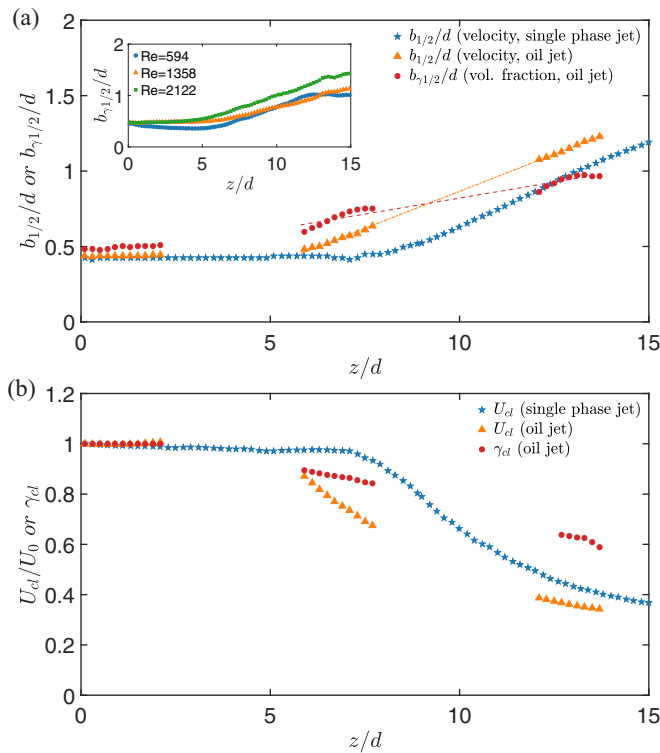


FIG. 4. (a) Axial development of the jet half widths with distance calculated from the velocity,  $b_{1/2}$ , for the single-phase and oil jet or the oil volume fraction,  $b_{\gamma_{1/2}}$ . Dashed lines are added to show trends. Inset shows the axial development of the  $b_{\gamma_{1/2}}$  of different jet Reynolds numbers calculated from PLIF data from Ref. [41], and (b) axial development of the jet centerline velocity,  $U_{cl}$ , normalized by jet mean centerline exit velocity:  $U_0 = 4.2$  m/s for oil jet, and 0.8 m/s for single-phase jet or the centerline oil fraction,  $\gamma_{cl}$ .

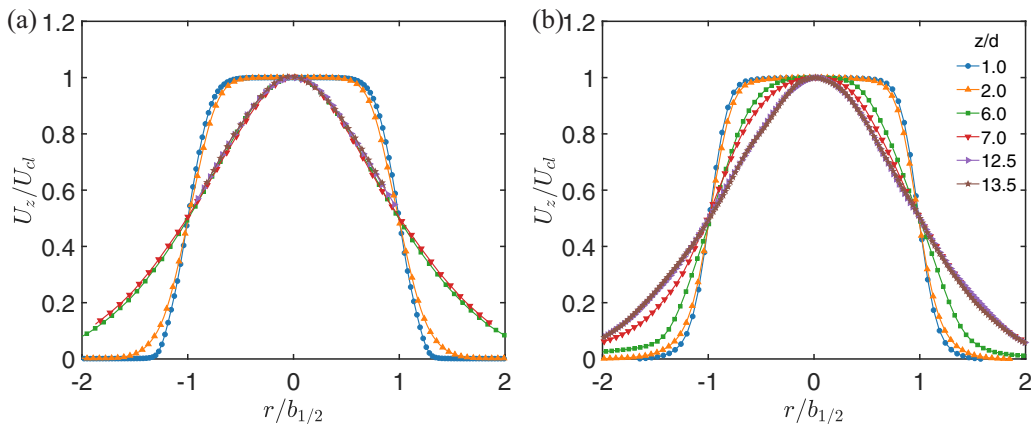


FIG. 5. Radial profiles of mean axial velocity normalized by the local centerline velocity,  $U_{cl}$ , and velocity half width,  $b_{1/2}$ : (a) oil jet in water, and (b) single-phase jet.

single-phase jet. The growth rate of the oil fraction half width is different. Near the nozzle,  $b_{\gamma 1/2}$  increases slightly but remains close to  $0.5d$ . Then, it increases at a faster rate than the velocity half width up to  $z/d = 5.8$ . In the  $z/d = 5.7-7.8$  range, both half widths increase at rates that are not significantly different, with  $b_{\gamma 1/2} > b_{1/2}$ . Further downstream, while  $b_{1/2}$  keeps on growing linearly, the growth rate of  $b_{\gamma 1/2}$  decreases, resulting in  $b_{\gamma 1/2}$  being smaller than  $b_{1/2}$  at  $z/d > 11.9$ . The ratio of the oil half widths, namely,  $\lambda = b_{\gamma 1/2}/b_{1/2}$ , averaged over the measurement domains decreases from 1.2 at  $z/d = 5.7-7.8$  to 0.8 at  $z/d = 11.9-13.8$ . The present value of  $\lambda$  at  $z/d = 5.7-7.8$  is consistent with those ( $\lambda \approx 1.2$ ) of some miscible buoyant jets and plumes [14,45,54,55], and higher than  $\lambda \approx 1$  reported by [10]. Yet, in all these miscible jet studies,  $\lambda$  remains above 1 further downstream, i.e., significantly larger than the present value at  $z/d = 11.9-14$ . Accordingly, between  $z/d = 5.7-13.8$ , the presently measured spreading and decay rates of the oil volume fraction,  $S = 0.042$  and  $C = 0.07$ , are smaller than those ( $S = 0.047-0.071$ ,  $C = 0.07-0.23$ ) reported for the miscible jet [13,56]. A likely reason for the different trends involves the buoyancy effect associated with the persistent presence of droplets. While the two fluids mix irreversibly in the miscible jet, causing a reduction in the effect of buoyancy, the cloud of droplets evident at  $z/d = 11.8-13.8$  persists, and continues to be influenced by buoyancy. Hence, the oil droplets continue to rise at a faster rate than the surrounding liquid and are less prone to diffuse radially outward. Since the droplet rise velocity increases with diameter, one would expect that an immiscible jet with weaker buoyancy effect, e.g., having smaller droplets, would spread at a faster rate. With increasing Reynolds number, the size of the droplet decreases, as shown for the present jet geometry in Ref. [41], consistent with prior studies [4,33]. Consequently, the oil jet should spread at a faster rate with increasing Reynolds number. Indeed, as shown in the inset presented in Fig. 4(a) for the experiments described in Ref. [41], which provide data for phase and size distributions, but do not involve velocity measurements,  $b_{\gamma 1/2}$  at  $Re = 2122$  is higher than those with the lower Reynolds numbers. The effects of buoyancy and droplet size on the relative velocity between phases will be further discussed in Sec. III C.

As demonstrated in Fig. 5(a), although the present measurements focus on the near field, the normalized radial profile of the mean axial velocity of the oil jet,  $U_z(r, z)/U_{cl}(z)$ , still collapses at  $z/d \geq 6$ ; namely, it appears to develop a self-similar behavior. The top-hat profiles are only limited to the very near field, as shown for  $z/d = 1$  and 2. In this range, the mean shear is concentrated along the jet perimeter. Since the spreading of the single-phase jet starts later, its profiles at  $z/d = 6$  and 7 have not reached a self-similar state [Fig. 5(b)]. However, once it does, its normalized profiles at  $z/d = 12.5$  and 13.5 collapse, and furthermore, appear to have a very similar shape as that of the

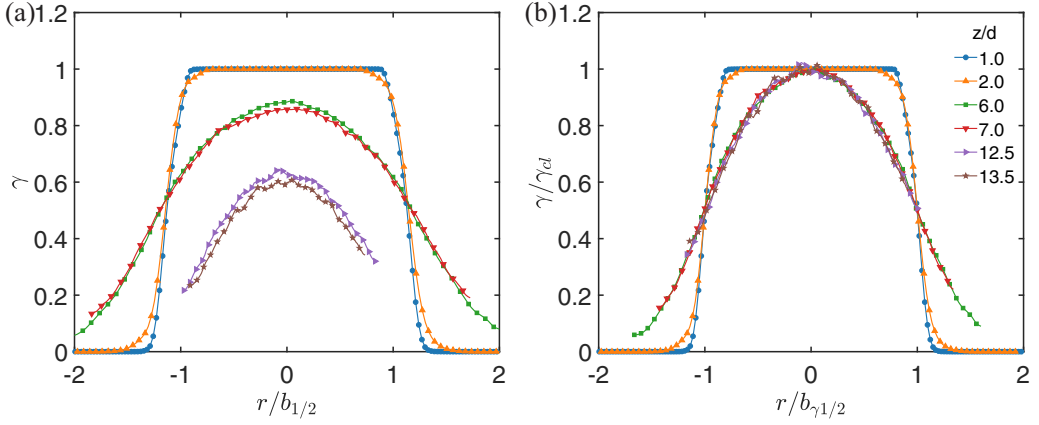


FIG. 6. Radial profiles of the oil volume fraction: (a) radial location is normalized by velocity half width,  $b_{1/2}$ , and (b) same data with the fraction normalized by local centerline value  $\gamma_{cl}$ , and radial location normalized by fraction half width  $b_{\gamma 1/2}$ .

self-similar oil jet. Hence, the evolution of the mean velocity can be characterized based on  $b_{1/2}$  and  $U_{cl}$ . The profiles of oil volume fraction plotted vs  $r/b_{1/2}$  are presented in Fig. 6(a), and the same data normalized by  $\gamma_{cl}$  and plotted vs  $r/b_{\gamma 1/2}$  are shown in Fig. 6(b). The top-hat profiles are confined to the very near field. At  $z/d > 6$ , all the void fraction profiles collapse; hence their trends could be characterized based on  $b_{\gamma 1/2}$  and  $\gamma_{cl}$ . However, note that the shape of the velocity profiles differs from those of the void fraction. The latter decay at a faster rate along the jet periphery; namely, the oil phase is more concentrated near the center of the jet than the jet momentum. Accordingly, the phase profiles are more rounded near the center. The impact of the differences between  $b_{1/2}$  and  $b_{\gamma 1/2}$  is demonstrated in Fig. 5(a), where  $\lambda > 1$  at  $z/d = 6-7$  implies a broader distribution, and  $\lambda < 1$  at  $z/d = 12.5-13.5$  indicates that the oil is predominantly concentrated near the center of the jet.

## B. Turbulence statistics

To provide insights for the dynamics that arise within the immiscible buoyant jet, we combine the phase distribution data obtained from the refractive index-matched PLIF data to the measurements of the velocity field. Following Ref. [55], the instantaneous velocity field is interrogated using a Heaviside step function,  $H(r, z, t)$ , whose value is unity in the oil and zero in the water. Then the phase-conditioned ensemble-averaged velocity in the oil,  $U_{i,o}(r, z)$ , and in the water,  $U_{i,w}(r, z)$ , are defined as

$$U_{i,o}(r, z) = \frac{1}{\sum H} \sum_{p=1}^M H(r, z, t_p) u_i(r, z, t_p) \quad (1)$$

and

$$U_{i,w}(r, z) = \frac{1}{M - \sum H} \sum_{p=1}^M [1 - H(r, z, t_p)] u_i(r, z, t_p), \quad (2)$$

where  $M$  is the total number of measurements at each location. Similarly, to examine the fluctuating velocity components, i.e.,  $u_i' = u_i - U_i$ , in each phase, the rms values of the velocity fluctuations

are

$$\langle u'_{i,o} u'_{j,o} \rangle = \frac{1}{\sum H} \sum_{p=1}^M H(r, z, t_p) u'_i(r, z, t_p) u'_j(r, z, t_p) \quad (3)$$

and

$$\langle u'_{i,w} u'_{j,w} \rangle = \frac{1}{M - \sum H} \sum_{p=1}^M [1 - H(r, z, t_p)] u'_i(r, z, t_p) u'_j(r, z, t_p), \quad (4)$$

where  $\langle \rangle$  indicates ensemble averaging. The Reynolds averaged momentum equation for each phase, neglecting the viscous terms, can be written as [57,58]

$$\frac{\partial(\gamma U_{i,o} U_{j,o})}{\partial x_i} = -\frac{1}{\rho_o} \frac{\partial(\gamma p)}{\partial x_j} - \frac{\partial(\gamma \langle u'_{i,o} u'_{j,o} \rangle)}{\partial x_i} + K_{i,o} + g_i \quad (5)$$

and

$$\frac{\partial[(1-\gamma)U_{i,w}U_{j,w}]}{\partial x_i} = -\frac{1}{\rho_w} \frac{\partial[(1-\gamma)p]}{\partial x_j} - \frac{\partial[(1-\gamma)\langle u'_{i,w}u'_{j,w} \rangle]}{\partial x_i} - K_{i,o} + g_i, \quad (6)$$

where the  $K_{i,o}$  is the so-called interaction term accounting for the effect of the water phase on the momentum of the oil. Combining the momentum equations for both phases, the fraction weighted Reynolds stresses then becomes

$$\langle \widetilde{u'_i u'_j} \rangle = \gamma \langle u'_{i,o} u'_{j,o} \rangle + (1-\gamma) \langle u'_{i,w} u'_{j,w} \rangle, \quad (7)$$

The discussion starts with a comparison between the fraction weighted Reynolds stresses of the oil jet and those of the single-phase jet. The left column of Fig. 7 shows the axial evolution of the profiles of  $\langle u'_z u'_z \rangle^{1/2}$ ,  $\langle u'_r u'_r \rangle^{1/2}$ ,  $\langle u'_z u'_r \rangle$ , and the right column displays the corresponding results for the single-phase jet. In general, the scaled near field turbulence in the oil jet is significantly higher than that in the single-phase jet, but the difference between them decreases with increasing  $z/d$ . Initially, both the axial and radial components of the turbulence have peaks coinciding with the azimuthal shear layer along the periphery of the jet. Further downstream, the location of the highest turbulence level shifts to the center of the jet. This transition occurs between  $z/d = 6$  and  $7$  for the oil jet and further downstream for the single-phase jet. For the latter, both the transition and the magnitude of the turbulence components are consistent with previously published results at similar Reynolds numbers [53]. Also, for both jets, the scaled axial and radial rms values increase with  $z/d$ , but this increase diminishes at  $z/d = 12.5-13.5$ , especially for the oil jet. It appears that in this range, the two profiles already collapse, indicating that the streamwise (and radial) velocity fluctuations can already be scaled using  $b_{1/2}$  and  $U_{cl}$ . Even at this location, the centerline axial rms peak of the oil jet, being around 0.29, is higher than that of the single-phase jet by about 14%, but the radial peak ( $\sim 0.21$ ) of the oil jet is only slightly higher. For both cases and at all locations, the radial fluctuations are smaller than the axial ones, also consistent with published results for single-phase jets [9,52].

The scaled Reynolds shear stresses [Figs. 7(e) and 7(f)], as expected, show growing double peaks near the jet periphery, with the centerline value being zero. Similar to the normal components, the shear stresses in the oil jet are higher than those in the single-phase jet at all elevations, but the difference between them decreases with increasing  $z/d$ . The maximum value for the single-phase jet at  $z/d = 12.5-13.5$ , 0.021, is in good agreement with previous results [9,52]. At  $z/d = 1$  and  $2$ , the single-phase values are very small, indicating that the flow there is essentially laminar. In the oil jet, entrainment of the surrounding water, the formation of ligaments, and the previously discussed vortices [Fig. 3] already result in low magnitude stresses of about  $1.6 \times 10^{-3}$ , which are highlighted in the inset.

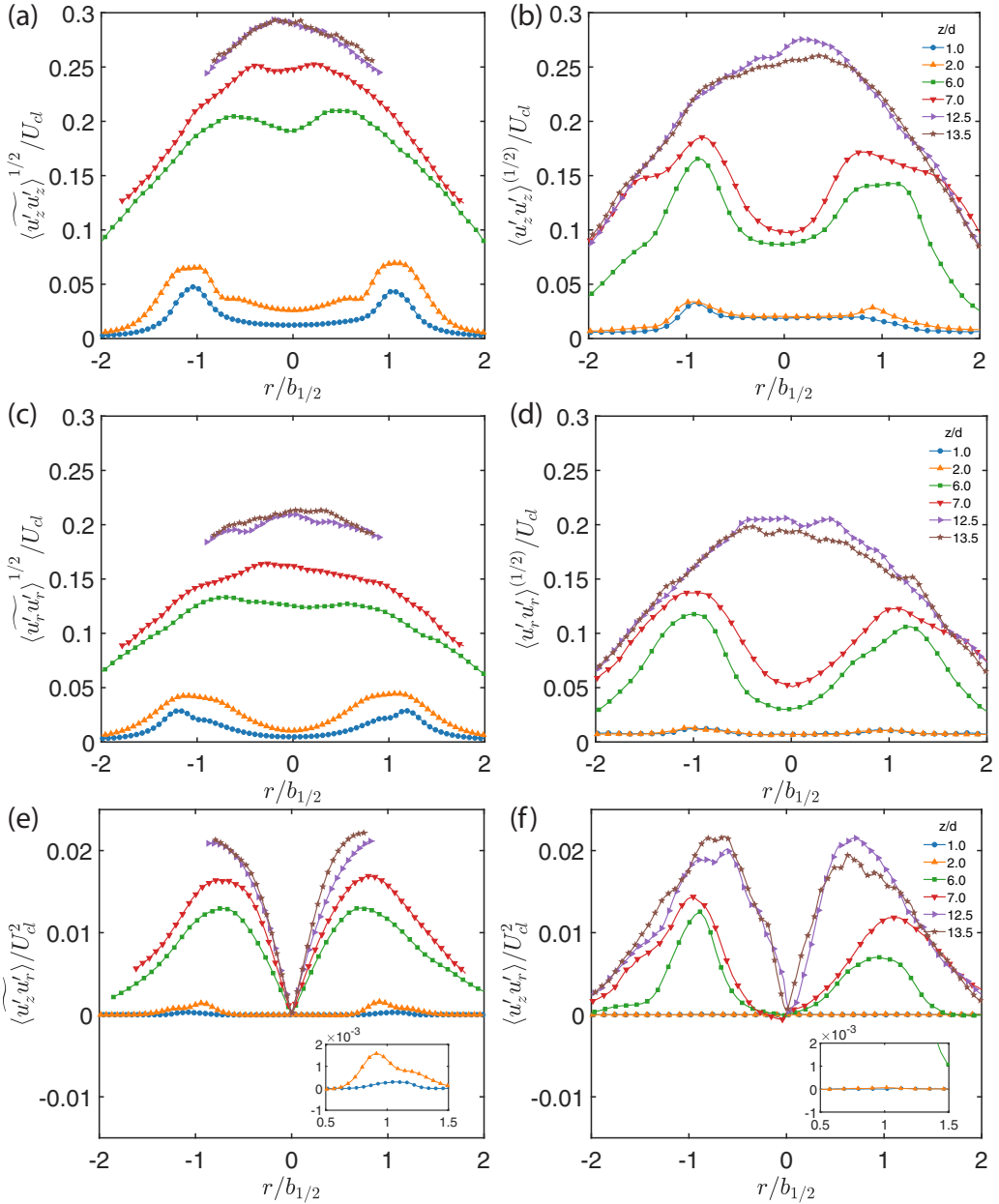


FIG. 7. Radial profiles of the (a), (b) axial rms velocity; (c), (d) radial rms velocity; and (e), (f) Reynolds shear stress normalized by  $U_{cl}$  and  $b_{1/2}$ . Left column (a), (c), (e): oil jet in water, and right column (b), (d), (f): single-phase jet. Insets show the magnified Reynolds shear stress at  $z/d = 1$  and  $2$ .

Another notable difference between the jets is the secondary hump in the  $\langle u'_z u'_z \rangle^{1/2}$  profile of the single-phase jet at  $z/d = 7$ , which does not appear a short distance upstream ( $z/d = 6$ ). Examination of the instantaneous realizations indicates that this phenomenon is associated with the pairing of the KH vortex that occurs preferentially at this elevation. As demonstrated in Figs. 8(a) and 8(b), [also see the swirling strength in Figs. 8(c) and 8(d)], while the vortices start to roll up at a lower elevation, they do not begin to pair until  $z/d = 6.8-7.4$ . Here, Figs. 8(b) and 8(d)

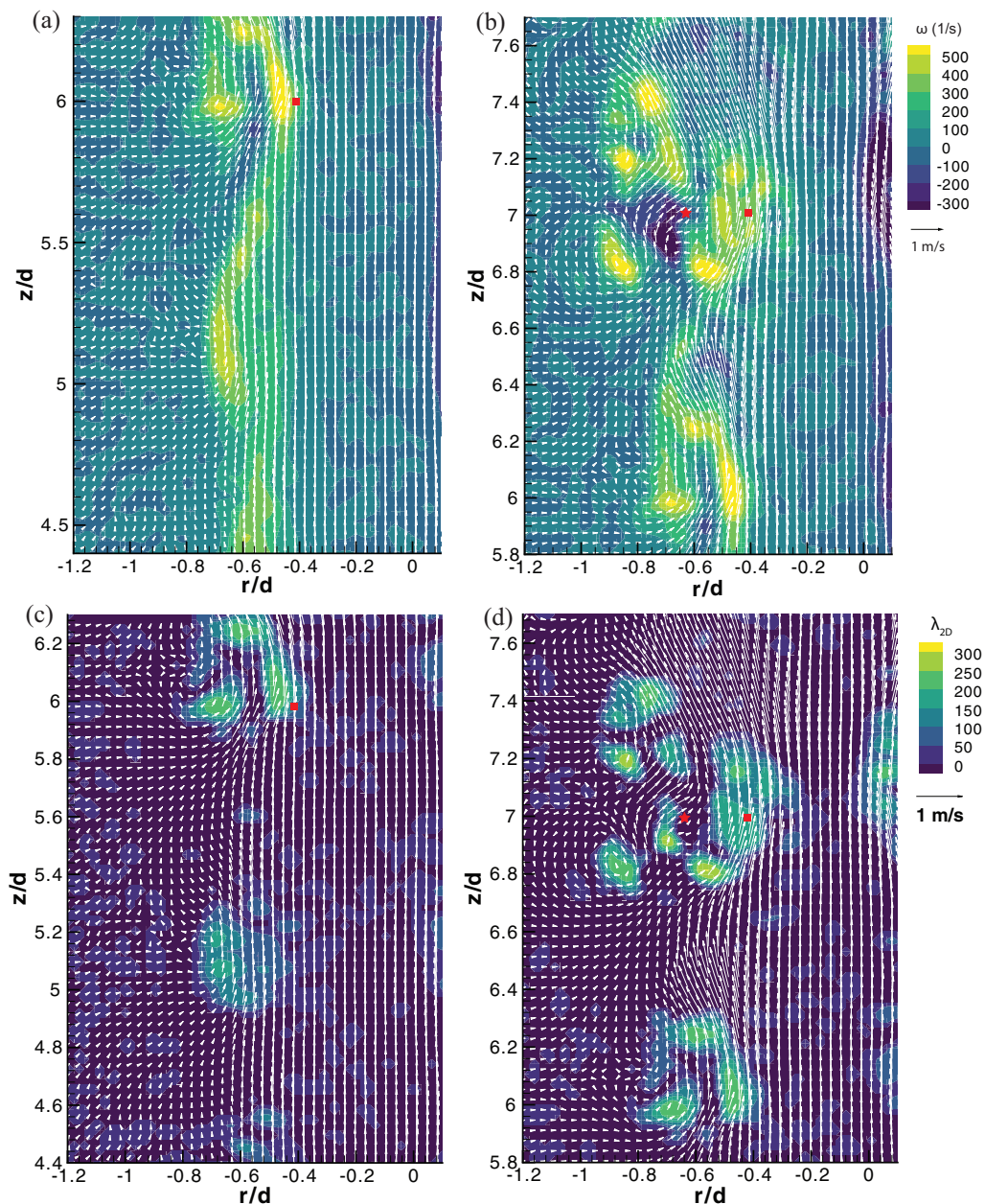


FIG. 8. Single-phase jet velocity vector overlaid with the (a), (b) vorticity magnitude; (c), (d) swirl strength. (a), (c)  $z/d = 4.4-6.3$ , and (b), (d)  $z/d = 5.8-7.7$ . The primary and secondary peak locations in the rms velocity are shown by the square and star symbols. Vectors in both figures are diluted and rescaled for clarity.

show multiple distinct clusters of vorticity and swirl strength peaks, with one of them being pushed radially inward to  $r/d = -0.55$ , and the others being pushed outward to  $r/d > 0.7$ . Such pairing and formation of clusters has been seen also in prior studies involving jets (e.g., Ref. [59]). The locations of  $\langle u'_z u'_z \rangle^{1/2}$  peaks and humps, which are marked with red symbols, can be used for comparing the scaled profiles to the physical ones. Further downstream, the secondary hump no longer exists beyond the potential core of the jet. These phenomena are not observed in the oil jet.

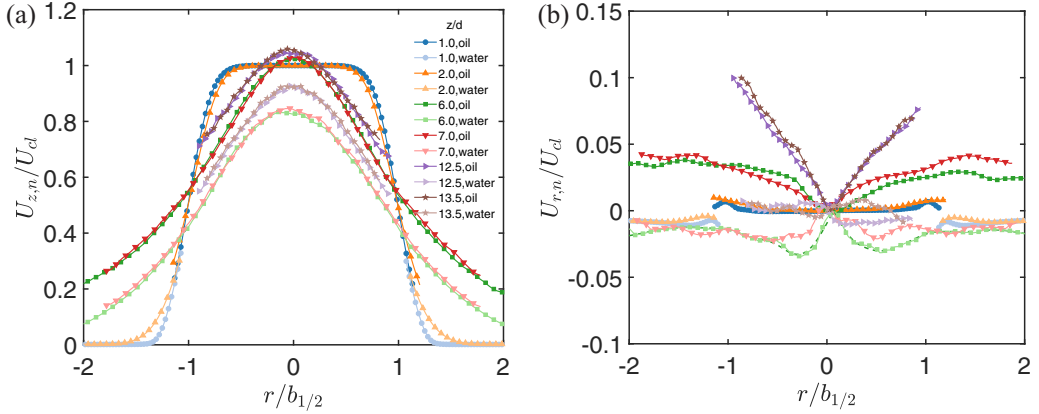


FIG. 9. Radial profiles of (a) the axial mean velocity, and (b) radial mean velocity with different downstream location, conditioned on the local presence of oil or water phase. Dashed line shows a spline fit of the radial mean velocity in water.

### C. Phase-dependent statistics

To investigate the contribution of each phase to the mean velocity profiles, Fig. 9 compares the axial evolution of the normalized mean velocity profiles of the two phases. Owing to the differences in magnitude, the streamwise velocity plots appear to be smooth, but the radial ones jitter, in part due to the uncertainty limit ( $\sim 10\%$  of  $U_0$ ), and in part due to the limited sample size of water in the middle of the jet, and oil along the periphery. Close to the nozzle, at  $z/d = 1$  and 2, the streamwise velocity profile of the oil remains a flat top, and there is a very small overlap with the water along the jet periphery. The water in this overlap region has nearly the same axial velocity as that of the oil. However, at  $z/d = 2$ , the velocity of the oil is slightly larger than that of the water (by 7% of  $U_{cl}$ ). The corresponding radial velocity profiles [Fig. 9(b)] indicate that the oil radial velocity is essentially zero in the jet core with a slight increase near  $r/b_{1/2} = \pm 1$ . In contrast, the radial water velocity outside the jet remains negative, presumably owing to entrainment, with a slight magnitude increase in the overlap region. Hence, in the small overlap region, the oil is moving radially outward while the water is moving inward. This trend persists at  $z/d = 6$  and 7, where some water has already penetrated to the center of the jet [Figs. 2(c) and 2(d)]. Here, the oil has a significantly higher axial velocity than that of the water across the entire jet, but the profiles of each phase nearly collapse. The difference between the phase velocity varies with radial location, peaking at 18% near the center, and being the smallest (11% of  $U_{cl}$ ) at  $r/b_{1/2} = \pm 0.75$ . Presuming that the interaction between phases is associated with drag, the momentum transfer between phases should peak near the center. As the scaled magnitudes of the radial velocity of both phases increase at  $z/d = 6$  and 7, the difference in their direction persists. The oil is dispersed outward, and its velocity increases with  $r/b_{1/2}$  near the center, and then plateaus at  $|r/b_{1/2}| > 1.2$ . In contrast, the water is moving inward, and its velocity magnitude at  $z/d = 6$  peaks at  $r/b_{1/2} \approx \pm 0.5$ . At  $z/d = 7$ , the peaks are less distinct and have lower magnitudes.

As the oil continues to break up into droplets by  $z/d = 12.5$  and 13.5, its streamwise velocity remains higher than that of the water, but the difference between them (13% of  $U_{cl}$ ) does not vary significantly in the radial direction. This velocity difference can be explained in terms of buoyancy effects as follows: The Sauter mean diameter of the droplets,  $D_{32}$ , is defined as  $D_{32} = (\int_0^\infty D_a^3 N' dD_a) / (\int_0^\infty D_a^2 N' dD_a)$ , where  $N'$  is the number density distribution [46]. Here, the apparent diameter,  $D_a$ , is calculated based on the total cross-sectional area of the droplets, including the water pockets if the droplet is compound. Integrating the blob size distribution presented in Fig. 10 gives  $D_{32} = 8.7$  mm. These oil patches are substantially larger than those measured further

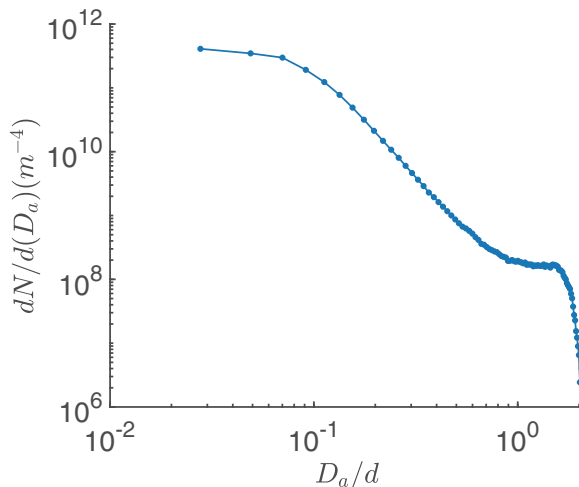


FIG. 10. Number density distribution of oil blobs at  $z/d = 11.8\text{--}13.8$ .

downstream under the same conditions, e.g.,  $D_{32} = 1.8$  mm at  $z/d = 30.6$  [41], indicating that the breakup process is still ongoing. Following the discussions in Refs. [60,61], the corresponding rise velocity in quiescent flows is  $U_q = 0.15$  m/s. In a turbulent flow with  $\langle \widetilde{u'_z u'_z} \rangle^{1/2} / U_q \approx 2$ , which corresponds to the present conditions, the mean rise velocity increases to 0.19 m/s. The latter is consistent with the measured average difference between the mean axial velocity of the two phases (0.20 m/s); i.e., this difference is driven by buoyancy and enhanced by turbulence.

Finally, at  $z/d = 12.5$  and  $13.5$ , the radial velocity of water, i.e., its entrainment rate, diminishes as the water fraction reaches nearly 40% [Fig. 6(a)] near the jet centerline. While the scaled radial oil velocity is higher than those measured at lower  $z/d$ , its actual magnitude is lower. This radial oil outflux should be expected since the oil fraction and (absolute) axial velocity keep on decreasing in this region. In fact, the measured values of  $\partial(\gamma U_{z,o})/\partial z$  match that of  $\partial(\gamma r U_{r,o})/r \partial r$  to within 15% (not shown), owing to combined effects of uncertainty in velocity (radial component, mostly) and volume fraction. The axial velocity of the water also decreases, but its fraction increases, resulting in a low radial influx.

The phase-conditioned radial profiles of the normal, and shear Reynolds stresses are plotted in Fig. 11. Here again, the jitter of the water data near the jet centerline at  $z/d = 6\text{--}7$  is attributable to the limited fraction of water there. The differences between Reynolds stress components of oil and water vary with elevation. At  $z/d = 1$  and  $2$ , in the narrow overlap region, where the oil ligaments form and entrain water,  $\langle u'_{z,w} u'_{z,w} \rangle^{1/2}$  and to a lesser extent  $\langle u'_{z,w} u'_{r,w} \rangle$  of the water are slightly higher than those of the oil. At  $z/d = 1$ , the radial velocity fluctuations peak in the water region where vortices form around the ligament tips, but the profiles of the oil and water almost collapse in the overlap region. At  $z/d = 2$ , it appears that the peaks in  $\langle u'_{z,o} u'_{r,o} \rangle$  and  $\langle u'_{z,w} u'_{r,w} \rangle$  do not coincide, indicating that the former is mostly contained in the azimuthal shear layer within the oil [Fig. 3(b)], whereas the latter is centered in the ligament-water vortex region [Fig. 3(a)]. For these reasons, the combined stress [Fig. 7(d)] has two humps. At  $z/d = 6$  and  $7$ , the trends are reversed, and the differences between the normal and shear stress in the water and the oil become significantly more substantial. The axial fluctuations and shear stresses in the oil are almost always higher than those of the water. In contrast, while the radial velocity fluctuations in the oil are higher along the jet periphery, those of the water are higher at the center. The following discussion will show that the latter trend can be attributed to the difference in the corresponding turbulence production rates. As the oil phase breaks up into droplets at  $z/d = 12.5$  and  $13.5$ , the differences between all the stress components in the oil and those in the water and near the center of the jet nearly diminish, and the distributions scaled using  $b_{1/2}$  and  $U_{c1}$  for each phase appear to collapse.

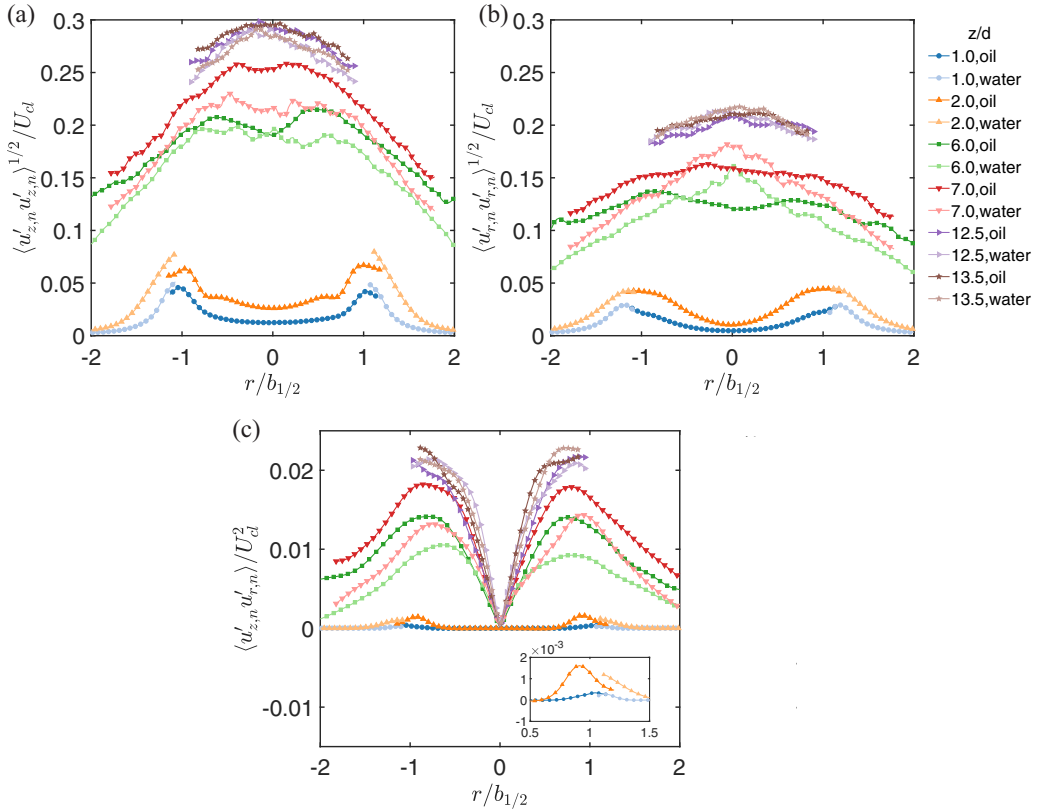


FIG. 11. Radial profiles of (a) the axial rms velocity; (b) radial rms velocity, and (c) Reynolds shear stress with different downstream location, conditioned on the local presence of oil or water phase. Insets show the magnified Reynolds shear stress at  $z/d = 1$  and  $2$ .

The next discussion investigates the reason why the turbulence level in the oil is higher than that in the water along the jet periphery at  $z/d = 6$  and  $7$ . Potential buoyancy effects, such as variations in the rise velocity of droplets (and blobs) with size in regions where they are sparse, are examined first. Figure 12 presents the joint probability density function (PDF) of the oil blob equivalent diameter,  $D_e/d$ , and the axial and radial velocity components of the oil blobs,  $u_{i,\text{blob}}/U_{cl}$ . Here,  $D_e$  is defined as the diameter of a circle with the same area as the cross section of the oil, regardless of whether it is compound or not, and  $u_{i,\text{blob}}$  is calculated by spatially averaging all the instantaneous velocity vectors within this blob. Only oil patches with centers located at  $r/b_{1/2} > 0$  are included. As is evident, while the blob population becomes broader and its concentration increases with decreasing  $D_e$ , the conditionally averaged values of  $u_{z,\text{blob}}/U_{cl}$  increase with the oil blob diameter. The joint PDF of the radial velocity component scatters in a similar fashion, yet the conditionally averaged distribution of  $u_{r,\text{blob}}$  remains nearly zero across the entire size spectrum. The difference between the trends of the two velocity components indicates that there is a clear buoyancy effect on the axial velocity component of the oil. However, since the radial velocity is not dependent on size, yet the oil radial fluctuations are higher than those of the water, the difference is not associated with blob size. Furthermore, the variance in velocity (either component) for oil blobs of similar size is much larger (98%) than the variations with oil patch size. Hence, buoyancy is not the cause of the higher level of peripheral turbulence in the oil.

The next step examines the impact of turbulence intermittency, especially in the water, resulting from entrainment of low momentum water into the jet. Besides the oil-water interface, another

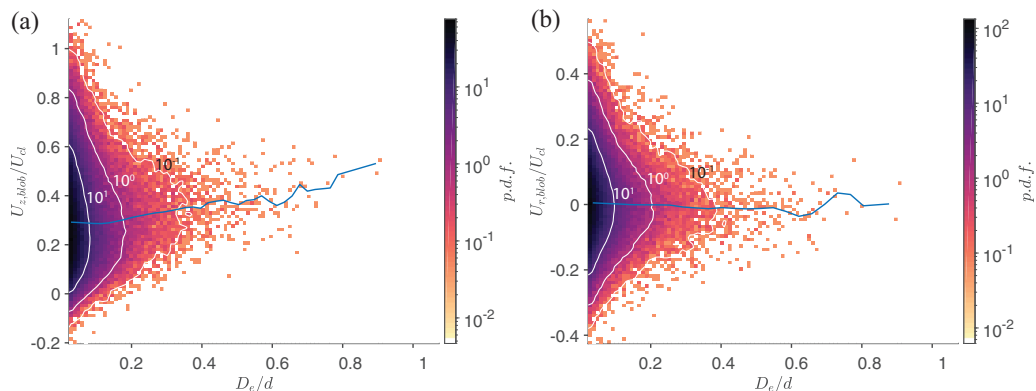


FIG. 12. The probability distributions of (a) the oil blob axial velocity, and (b) oil blob radial velocity with respect to the equivalent blob diameter for  $z/d = 5.7-7.8$ . The blue lines show the averaged velocity components for each diameter. Only the oil blobs which located outside the jet (radial location of the blob's center of mass larger than  $b_{1/2}$ ) are included.

distinct feature along the jet periphery is the presence of a turbulent/nonturbulent interface (TNTI) [62]. Here, we use the normalized vorticity as a criterion for separating vortical (i.e., turbulent) regions from the surrounding irrotational flow, as suggested by Ref. [63]. For free shear flows, including jets, the recommended normalization for each elevation ( $z_0$ ) is

$$|\omega|^+(r, z_0, t) = \frac{|\omega|(r, z_0, t)}{\max[|\omega'(r, z_0)\omega'(r, z_0)|^{1/2}]}. \quad (8)$$

Here  $|\omega| = (\omega_\theta \omega_\theta)^{1/2}$  is the instantaneous circumferential vorticity magnitude, and the denominator is the maximum rms value of the vorticity along with the radial profile. Following Ref. [64], the threshold should be selected as the inflection point in the vorticity magnitude histogram for the entire sample volume. Based on the present data (not shown),  $|\omega|^+ = 0.5$  has been selected as the threshold. Therefore, an additional step function,  $I(r, z, t)$ , is defined, whose value is unity for  $|\omega|^+ > 0.5$  (“turbulent region”) and zero where  $|\omega|^+ \leq 0.5$ . Partitioning the jet flow by combining the phase distribution and turbulent regions, four zones can be delineated: (i) turbulent and oil:  $I(r, z, t)H(r, z, t) = 1$ ; (ii) nonturbulent and oil:  $[1 - I(r, z, t)]H(r, z, t) = 1$ ; (iii) turbulent and water:  $I(r, z, t)[1 - H(r, z, t)] = 1$ ; and (iv) nonturbulent and water:  $[1 - I(r, z, t)][1 - H(r, z, t)] = 1$ . The corresponding fractions for each zone can then be determined by ensemble averaging. For example, for a turbulent zone containing oil,

$$\chi_{T,o} = \frac{1}{M} \sum_{p=1}^M I(r, z, t_p)H(r, z, t_p), \quad (9)$$

where  $M$  corresponds to the total number of samples at a given location. The rest of the fractions are determined in the same manner.

Figure 13(a) shows the fraction budgets at  $z/d = 6$ . For the oil phase, the turbulent fraction peaks at  $r/b_{1/2} = \pm 0.5$ , at the same locations as the corresponding peaks in  $\langle u'_{z,o} u'_{r,o} \rangle$  [Fig. 11(a)]. The oil in the centerline is less turbulent. Here,  $\chi_{T,o}$  is 0.43, slightly lower than the nonturbulence fraction (0.45). At  $r/b_{1/2} > \pm 1$ , both the turbulent and nonturbulent oil fractions diminish due to the decreasing oil fraction. For the water phase, the turbulent peaks are centered around  $r/b_{1/2} = \pm 1.4$ , i.e., outward from those of the oil, and from the jet half width. Near the centerline, the fraction of nonturbulent water is almost zero, but it increases rapidly at  $r/b_{1/2} > 1.0$ . Another convenient approach for examining the trends of intermittency is based on calculating the fraction of turbulent

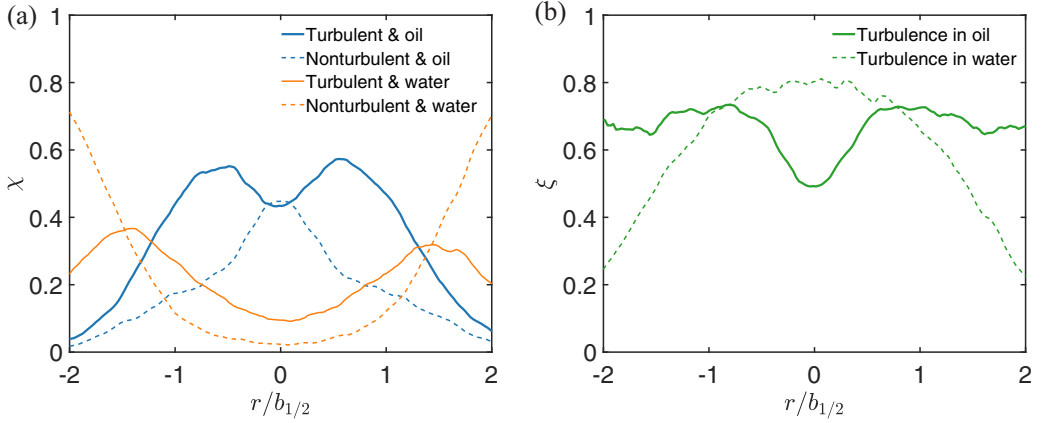


FIG. 13. Radial profiles of (a) the fraction budget of the turbulent and nonturbulent, and oil and water phase zones at  $z/d = 6$ , blue: oil phase; orange: water phase; solid line: turbulent; dashed line: nonturbulent. The fractions add up to 1 for a given radial location, and (b) fraction of turbulent zones in oil (solid) and in water (dashed).

regions in each phase separately using

$$\xi_o = \frac{1}{\sum H} \sum_{p=1}^M I(r, z, t_p) H(r, z, t_p) \quad (10)$$

and

$$\xi_w = \frac{1}{M - \sum H} \sum_{p=1}^M I(r, z, t_p) [1 - H(r, z, t_p)]. \quad (11)$$

The results, presented in Fig. 13(b), indicate that near the center of the jet, a little less than 50% of the oil is turbulent, but this fraction increases along the perimeter and remains high. In contrast, while the water blobs entrained into the center are mostly turbulent, the fraction of turbulent zones decreases rapidly with increasing  $r/d$ . Therefore, substantial fractions of ambient water penetrating into the jet are still not turbulent, resulting in lower axial and radial velocity fluctuations as well as shear stress along the periphery. However, while the turbulent fraction in the water is higher than that of the oil near the jet center, the oil streamwise velocity fluctuations [Fig. 11(a)], which are the largest component, are still higher than those of the water. These conflicting trends imply that the amplitude of fluctuations in the turbulent oil fraction must be higher than those in the water. In contrast, the water radial velocity fluctuations near the jet center are higher than those in the oil [Fig. 11(b)]. While being consistent with the trends of turbulent fractions, the reason for the different trends among the components is not clear. The next section attempts to provide a plausible explanation for this discrepancy by examining the corresponding turbulent production rates. Before concluding this section, it should be noted that the differences between turbulence levels have also been measured in the periphery of the far field of miscible buoyancy-driven liquid plumes [55]. In that study, in the outer perimeter, the axial velocity fluctuations are higher in the dispersed phase, consistent with the present finding. However, further inward (but far from the center), the trends are reversed. The authors postulate that the latter trend is a result of differences in the turbulence production rate.

#### D. Turbulent kinetic energy production

This section investigates the production rates of the turbulent kinetic energy (TKE) and normal Reynolds stress components as well as the flow phenomena affecting them. In multiphase flow

containing  $n$  phases with volume fraction fractions,  $\gamma_n$ , the TKE production rate derived from the Reynolds averaged momentum equation and expressed in a cylindrical coordinate system is

$$\begin{aligned} \tilde{P} = & - \sum_n \left[ \langle u'_{r,n} u'_{r,n} \rangle \frac{\partial \gamma_n U_{r,n}}{\partial r} + \langle u'_{z,n} u'_{r,n} \rangle \left( \frac{\partial \gamma_n U_{r,n}}{\partial z} + \frac{\partial \gamma_n U_{z,n}}{\partial r} \right) \right. \\ & \left. + \langle u'_{\theta,n} u'_{\theta,n} \rangle \frac{\gamma_n U_{r,n}}{r} + \langle u'_{z,n} u'_{z,n} \rangle \frac{\partial \gamma_n U_{z,n}}{\partial z} \right]. \end{aligned} \quad (12)$$

Since  $\langle u'_\theta u'_\theta \rangle$  is not measured, in the following analysis, it is assumed to be equal to  $\langle u'_r u'_r \rangle$ , i.e., assuming axial symmetry and isotropy. Many previous measurements [11,12,52,54] have shown that this assumption is reasonable for single-phase and buoyant jets. Using this assumption, the TKE and individual normal stress production rates of each phase are

$$P_n = - \left[ \langle u'_{r,n} u'_{r,n} \rangle \frac{\partial U_{r,n}}{\partial r} + \langle u'_{z,n} u'_{r,n} \rangle \left( \frac{\partial U_{r,n}}{\partial z} + \frac{\partial U_{z,n}}{\partial r} \right) + \langle u'_{r,n} u'_{r,n} \rangle \frac{U_{r,n}}{r} + \langle u'_{z,n} u'_{z,n} \rangle \frac{\partial U_{z,n}}{\partial z} \right], \quad (13)$$

$$P_{\langle u'_{r,n} u'_{r,n} \rangle} = -2 \left( \langle u'_{r,n} u'_{r,n} \rangle \frac{\partial U_{r,n}}{\partial r} + \langle u'_{z,n} u'_{r,n} \rangle \frac{\partial U_{r,n}}{\partial z} \right), \quad (14)$$

$$P_{\langle u'_{z,n} u'_{z,n} \rangle} = -2 \left( \langle u'_{z,n} u'_{r,n} \rangle \frac{\partial U_{z,n}}{\partial r} + \langle u'_{z,n} u'_{z,n} \rangle \frac{\partial U_{z,n}}{\partial z} \right), \quad (15)$$

$$P_{\langle u'_{\theta,n} u'_{\theta,n} \rangle} = -2 \langle u'_{r,n} u'_{r,n} \rangle \frac{U_{r,n}}{r}. \quad (16)$$

Since the calculations involve velocity gradients, which are sensitive to the jitter in the radial velocity distributions, their profiles are fitted with cubic smoothing splines, as illustrated in Fig. 9(b). For the azimuthal term near the jet centerline ( $\langle u'_{r,n} u'_{r,n} \rangle U_{r,n}/r$ ), the singularity is removed using L'Hôpital's rule. Figure 14(a) shows the radial profile of  $\tilde{P}$  and the terms contributing to it at  $z/d = 6$ . Here, data for both sides of the jet are combined. Evidently, the shear production term,  $\langle u'_{z,n} u'_{r,n} \rangle (\partial U_{r,n}/\partial z + \partial U_{z,n}/\partial r)$ , is the dominant contributor with a peak located near  $r/b_{1/2} = 0.78$ . While the axial term contributes to the centerline production, it becomes negative along the jet periphery. The radial and azimuthal components are both very small and negative near the center. The location of the total TKE production rate,  $r/b_{1/2} = 0.67$ , is not significantly different than that measured in the far field of single-phase jets [52]. While the present single-phase jet is still undergoing transition at  $z/d = 6$ , the peak TKE production of this jet at  $z/d = 13.5$  is also located at a similar radius ( $r/b_{1/2} = 0.61$ ).

The corresponding terms in each of the phases are compared in Fig. 14(b). As is evident, the shear and axial production rates in the oil are significantly higher than that in the water at all radial locations, especially near the corresponding peaks. There are also noticeable differences in the trends of the radial contraction ( $\langle u'_{r,n} u'_{r,n} \rangle \partial U_{r,n}/\partial r$ ) and azimuthal terms ( $\langle u'_{r,n} u'_{r,n} \rangle U_{r,n}/r$ ) near the center of the jet, with those of the oil being negative (but small), and those of the water being positive. The sign difference in radial production is caused by the radial contraction of the water and the radial extension of the oil. The difference in azimuthal terms is associated with the direction of the radial velocity components [Fig. 9(b)]. Consequently, the distributions of oil and water TKE production rates near the center of the jet take very different forms, with that of the water being almost five times higher. Consequently, as shown in Fig. 15, the turbulent kinetic energy in the water, estimated using  $k_n = (\langle u'_{z,n} u'_{z,n} \rangle + 2\langle u'_{r,n} u'_{r,n} \rangle)/2$ , is higher than that of the oil near the jet centerline. It might also explain the higher fraction of turbulent regions in the water compared to those in the oil near the center. In contrast, along the jet perimeter, the oil turbulence is higher, also consistent with the distribution of production rates. These observations imply that in addition to the previously discussed effects of intermittency, the lower turbulence level in the water along the periphery is also affected by the lower production rate there. Finally, it would also be interesting to compare the production rates of specific normal Reynolds stress components. The results, summarized in Fig. 16,

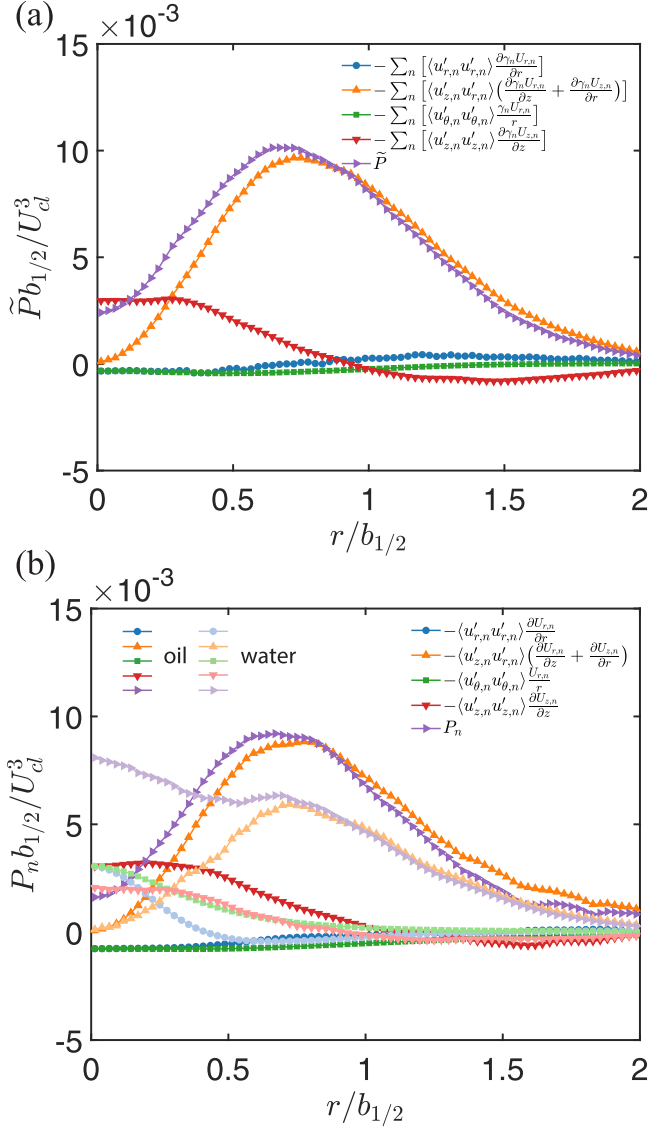


FIG. 14. Radial profiles of (a) the combined turbulent kinetic energy (TKE) production term and its components, and (b) TKE production term of each phase and its components at  $z/d = 6$ , dark line: oil phase; faded line: water phase.

demonstrate that while  $P_{\langle u'_{z,n} u'_{z,n} \rangle}$  of the oil is higher than that of the water along the entire jet radius,  $P_{\langle u'_{r,n} u'_{r,n} \rangle}$  and  $P_{\langle u'_{\theta,n} u'_{\theta,n} \rangle}$  of the water are positive, and those of the oil are negative in the vicinity of the jet centerline. These trends are consistent with those of the axial and radial velocity fluctuations as well as the turbulent fractions in each phase. For example, at  $z/d = 6$ ,  $\langle u'_{z,o} u'_{z,o} \rangle$  is almost equal to  $\langle u'_{z,w} u'_{z,w} \rangle$  and  $\langle u'_{r,o} u'_{r,o} \rangle < \langle u'_{r,w} u'_{r,w} \rangle$  near the centerline. Furthermore,  $\langle u'_{z,o} u'_{z,o} \rangle$  is significantly higher than  $\langle u'_{r,o} u'_{r,o} \rangle$  along the entire radius, with the difference reaching 58% along the centerline. Also,  $\langle u'_{r,w} u'_{r,w} \rangle$  has a sharp peak near the center, whereas  $\langle u'_{r,o} u'_{r,o} \rangle$  has a broad distribution; both are consistent with the trends of the corresponding production rates.

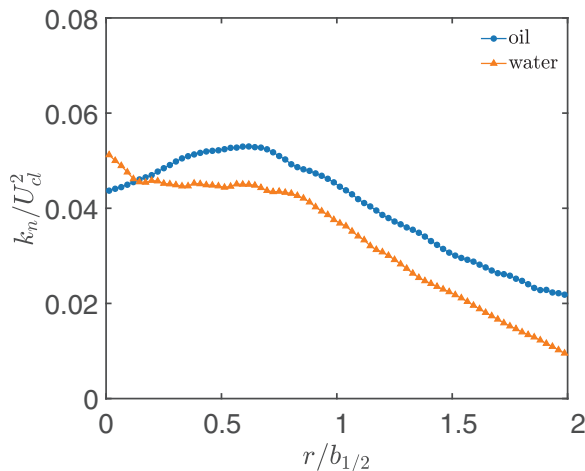


FIG. 15. Radial profiles of the turbulent kinetic energy of each phase at  $z/d = 6$ .

#### IV. SUMMARY AND CONCLUSIONS

This study examines the flow structure and turbulence in the near field of an immiscible buoyant oil jet injected into quiescent water at a low Reynolds number. Velocity and phase distribution measurements are performed simultaneously by applying particle image velocimetry, and planar laser-induced fluorescence in a refractive index-matched setup involving silicone oil and sugar water. These fluids have similar viscosity and density ratios, as well as the interfacial tension with those of crude oil and seawater. The results include distributions of the phase, number density of the droplet diameter, and profiles of the mean velocity; rms values of the axial and radial velocity fluctuations, and Reynolds shear stress. Data analysis examines the mean flow and turbulence structures in both phases separately and combined. Trends are compared to those of a single-phase jet at the same Reynolds number. The discussion attempts to elucidate causes for differences in the evolution of turbulent quantities between the oil and single-phase jets, the water and the oil in the immiscible jet, and among the normal Reynolds stress components.

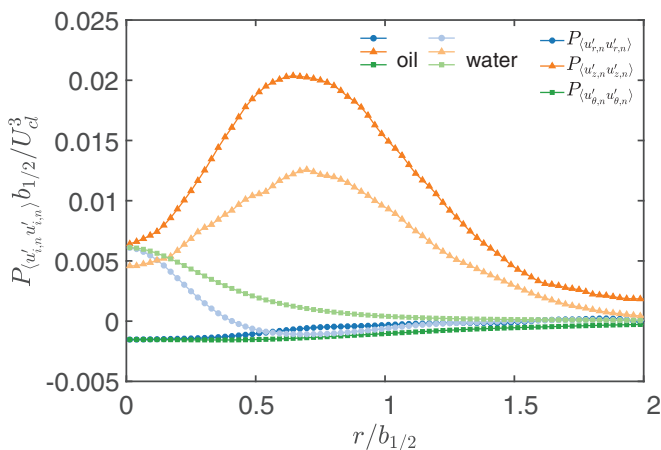


FIG. 16. Radial profiles of the normal Reynolds stress production term for each phase at  $z/d = 6$ . Dark line: oil phase; faded line: water phase.

In the azimuthal shear layer developing close to the nozzle exit, while some vertical momentum of the water is obtained by shear, significant gain occurs as thin water layers are entrained into the jet, while oil ligaments start to extend outward. Kelvin-Helmholtz vortices form in the water, with their centers located at the tip of the extended oil ligaments. Further downstream, as the oil breaks up into large blobs and subsequently to droplets, while entraining water, the axial momentum and oil-containing domain expand concurrently with a reduction in the centerline oil fraction and velocity. The spreading rate of the oil volume fraction and the decrease in its centerline concentration are lower than those of the axial momentum and centerline velocity. What appear to be universal profiles of either the phase distribution or the axial momentum that could be scaled with the half widths and centerline values develop at  $z/d = 6$ . In the single-phase jet, the transition from an azimuthal shear layer to a self-similar profile of velocity occurs further downstream. The mean axial velocity of the oil is always higher than that of the water, as expected for a buoyant jet. At  $z/d \geq 12.5$ , where the scaled profiles collapse, its normalized profiles appear to have a very similar shape as that of the self-similar oil jet. The difference between the axial velocities of the phases is consistent with the buoyant rise velocity of oil droplets with the same Sauter mean diameter in turbulent flows. The radial fluxes of the oil and water have opposite signs as the oil expands, and the water is entrained inward.

The turbulence level and shear stress in the oil jet are higher than those in the single-phase jet, but this difference decreases with increasing  $z/d$ . There are also significant disparities between the magnitude and trends of velocity fluctuations and shear stress between the two phases of the immiscible jet. Close to the nozzle, the velocity fluctuations and shear stress in the water are higher than those in the oil along the narrow phase-overlap region along the periphery of the jet. Consequently, the combined Reynolds stress profile has two peripheral humps, one corresponding to the shear layer within the oil, and an outer one in the region containing predominantly water.

At  $z/d = 6$ , where the oil velocity fluctuations still have a broad peak off the jet center, along the jet periphery, all the turbulent quantities are higher in the oil. Near the jet center, the water radial velocity fluctuations have a sharp peak with a magnitude that is higher than the corresponding levels in the oil. Several potential contributors are evaluated in attempts to explain the different trends. The higher oil turbulence along the jet periphery cannot be caused by size-dependent differences in the buoyant rise velocity of the oil blobs. However, it appears to be affected by turbulence intermittency in the water as quiescent outer fluid is entrained into the jet, as well as by the higher shear-dominated turbulence production rate in the oil. In contrast, near the jet center, the TKE production rate in the water is significantly higher than that in the oil. This latter trend is associated with radial contraction and inward flow of the water, which increase the turbulence production, as opposed to the radial extension of the oil, which decreases it.

Thirteen diameters downstream of the nozzle, where most of the oil is already fragmented into large droplets or blobs, the differences between oil and water turbulence levels diminish, and the scaled profiles of the normal and shear stresses in each phase nearly collapse. Still, the axial velocity fluctuations are substantially higher than the radial ones. The droplet size distributions measured under very similar conditions at  $z/d = 30.6$  [41] have a Sauter mean diameter that is five times larger than those at  $z/d = 13$ , indicating that the fragmentation of the oil persists well beyond the range examined in this paper. The relationship between this persistent fragmentation process and the evolution of the turbulence in the jet, as well as a broad range of Reynolds numbers including the turbulent exit flow, will be examined in subsequent studies.

Data are publicly available through the Gulf of Mexico Research Initiative Information and Data Cooperative (GRIIDC) at [65].

#### ACKNOWLEDGMENTS

This research was made possible in part by a grant from The Gulf of Mexico Research Initiative, and in part by the Multi-University Research Partnership (MPRI), Fisheries and Oceans, Canada.

The authors thank G. Tryggvason, R. Ni, C. Meneveau, and A. Aiyer for helpful comments and insights.

- 
- [1] N. Machicoane, J. K. Bothell, D. Li, T. B. Morgan, T. J. Heindel, A. L. Kastengren, and A. Aliseda, Synchrotron radiography characterization of the liquid core dynamics in a canonical two-fluid coaxial atomizer, *Int. J. Multiphase Flow* **115**, 1 (2019).
  - [2] A. W. Woods, Turbulent plumes in nature, *Annu. Rev. Fluid Mech.* **42**, 391 (2010).
  - [3] D. Yang, B. Chen, S. A. Socolofsky, M. Chamecki, and C. Meneveau, Large-eddy simulation and parameterization of buoyant plume dynamics in stratified flow, *J. Fluid Mech.* **794**, 798 (2016).
  - [4] Ø. Johansen, P. J. Brandvik, and U. Farooq, Droplet breakup in subsea oil releases—Part 2: Predictions of droplet size distributions with and without injection of chemical dispersants, *Mar. Pollut. Bull.* **73**, 327 (2013).
  - [5] L. Zheng, P. D. Yapa, and F. Chen, A model for simulating deepwater oil and gas blowouts—Part I: Theory and model formulation, *J. Hydraul. Res.* **41**, 339 (2003).
  - [6] S. A. Socolofsky, E. E. Adams, and C. R. Sherwood, Formation dynamics of subsurface hydrocarbon intrusions following the deepwater horizon blowout, *Geophys. Res. Lett.* (2011).
  - [7] L. Zhao, F. Shaffer, B. Robinson, T. King, C. D’Ambrose, Z. Pan, F. Gao, R. S. Miller, R. N. Conmy, and M. C. Boufadel, Underwater oil jet: Hydrodynamics and droplet size distribution, *Chem. Eng. J.* **299**, 292 (2016).
  - [8] P. E. Dimotakis and D. R. Dowling, Similarity of the concentration field of gas-phase turbulent jets, *J. Fluid Mech.* **218**, 109 (1990).
  - [9] H. J. Hussein, S. P. Capp, and W. K. George, Velocity measurements in a high-Reynolds-number, momentum-conserving, axisymmetric, turbulent jet, *J. Fluid Mech.* **258**, 31 (1994).
  - [10] H. Wang and A. W. K. Law, Second-order integral model for a round turbulent buoyant jet, *J. Fluid Mech.* **459**, 397 (2002).
  - [11] N. R. Panchapakesan and J. L. Lumley, Turbulence measurements in axisymmetric jets of air and helium. Part 1. Air jet, *J. Fluid Mech.* **246**, 197 (1993).
  - [12] A. Darisse, J. Lemay, and A. Benaïssa, Budgets of turbulent kinetic energy, Reynolds stresses, variance of temperature fluctuations and turbulent heat fluxes in a round jet, *J. Fluid Mech.* **774**, 95 (2015).
  - [13] J. J. Charonko and K. Prestridge, Variable-density mixing in turbulent jets with coflow, *J. Fluid Mech.* **825**, 887 (2017).
  - [14] A. Ezzamel, P. Salizzoni, and G. R. Hunt, Dynamical variability of axisymmetric buoyant plumes, *J. Fluid Mech.* **765**, 576 (2015).
  - [15] A. G. Mychkovsky and S. L. Ceccio, LDV measurements and analysis of gas and particulate phase velocity profiles in a vertical jet plume in a 2D bubbling fluidized bed. Part II: Mass and momentum transport, *Powder Technol.* **220**, 47 (2012).
  - [16] M. Wegener, J. Grünig, J. Stüber, A. R. Paschedag, and M. Kraume, Transient rise velocity and mass transfer of a single drop with interfacial instabilities—experimental investigations, *Chem. Eng. Sci.* **62**, 2967 (2007).
  - [17] K. J. Stebe and D. Barthès-Biesel, Marangoni effects of adsorption–desorption controlled surfactants on the leading end of an infinitely long bubble in a capillary, *J. Fluid Mech.* **286**, 25 (1995).
  - [18] K. D. Squires and J. K. Eaton, Particle response and turbulence modification in isotropic turbulence, *Phys. Fluids A* **2**, 1191 (1990).
  - [19] J. H. Lee and V. Chu, *Turbulent Jets and Plumes: A Lagrangian Approach* (Springer Science & Business Media, Berlin, 2012).
  - [20] V. Ferrand, R. Bazile, J. Borée, and G. Charnay, Gas-droplet turbulent velocity correlations and two-phase interaction in an axisymmetric jet laden with partly responsive droplets, *Int. J. Multiphase Flow* **29**, 195 (2003).

- [21] J. Feng and I. A. Bolotnov, Evaluation of bubble-induced turbulence using direct numerical simulation, *Int. J. Multiphase Flow* **93**, 92 (2017).
- [22] G. Bellani, M. L. Byron, A. G. Collignon, C. R. Meyer, and E. A. Variano, Shape effects on turbulent modulation by large nearly neutrally buoyant particles, *J. Fluid Mech.* **712**, 41 (2012).
- [23] J. Rensen and V. Roig, Experimental study of the unsteady structure of a confined bubble plume, *Int. J. Multiphase Flow* **27**, 1431 (2001).
- [24] B. Bunner and G. Tryggvason, Effect of bubble deformation on the properties of bubbly flows, *J. Fluid Mech.* **495**, 77 (2003).
- [25] B. R. Morton, G. Taylor, and J. S. Turner, Turbulent gravitational convection from maintained and instantaneous sources, *Proc. R. Soc. London, Ser. A* **234**, 1 (1956).
- [26] J. S. Turner, Turbulent entrainment: The development of the entrainment assumption, and its application to geophysical flows, *J. Fluid Mech.* **173**, 431 (1986).
- [27] G. G. Rooney and P. F. Linden, Similarity considerations for non-Boussinesq plumes in an unstratified environment, *J. Fluid Mech.* **318**, 237 (1996).
- [28] M. Van Reeuwijk and J. Craske, Energy-consistent entrainment relations for jets and plumes, *J. Fluid Mech.* **782**, 333 (2015).
- [29] P. Carlotti and G. R. Hunt, Analytical solutions for turbulent non-Boussinesq plumes, *J. Fluid Mech.* **538**, 343 (2005).
- [30] A. L. Dissanayake, J. Gros, and S. A. Socolofsky, Integral models for bubble, droplet, and multiphase plume dynamics in stratification and crossflow, *Environ. Fluid Mech.* **18**, 1167 (2018).
- [31] S. Balachandar and J. K. Eaton, Turbulent dispersed multiphase flow, *Annu. Rev. Fluid Mech.* **42**, 111 (2010).
- [32] A. K. Aiyer, D. Yang, M. Chamecki, and C. Meneveau, A population balance model for large eddy simulation of polydisperse droplet evolution, *J. Fluid Mech.* **878**, 700 (2019).
- [33] S. Saito, Y. Abe, and K. Koyama, Flow transition criteria of a liquid jet into a liquid pool, *Nucl. Eng. Des.* **315**, 128 (2017).
- [34] M. Landeau, R. Deguen, and P. Olson, Experiments on the fragmentation of a buoyant liquid volume in another liquid, *J. Fluid Mech.* **749**, 478 (2014).
- [35] M. C. Boufadel, S. Socolofsky, J. Katz, D. Yang, C. Daskiran, and W. Dewar, A review on multiphase underwater jets and plumes: Droplets, hydrodynamics, and chemistry, *Rev. Geophys.* **58**, e2020RG000703 (2020).
- [36] A. Lowe, A. Kourmatzis, and A. R. Masri, Turbulent spray flames of intermediate density: Stability and near-field structure, *Combust. Flame* **176**, 511 (2017).
- [37] P. Marmottant and E. Villermaux, On spray formation, *J. Fluid Mech.* **498**, 73 (2004).
- [38] J. C. Lasheras and E. J. Hopfinger, Liquid jet instability and atomization in a coaxial gas stream, *Annu. Rev. Fluid Mech.* **32**, 275 (2000).
- [39] O. Desjardins, J. O. McCaslin, M. Owkes, and P. Brady, Direct numerical and large-eddy simulation of primary atomization in complex geometries, *Atomization Sprays* **23**, 1001 (2013).
- [40] A. Aliseda, E. J. Hopfinger, J. C. Lasheras, D. M. Kremer, A. Berchielli, and E. K. Connolly, Atomization of viscous and non-Newtonian liquids by a coaxial, high-speed gas jet. Experiments and droplet size modeling, *Int. J. Multiphase Flow* **34**, 161 (2008).
- [41] X. Xue and J. Katz, Formation of compound droplets during fragmentation of turbulent buoyant oil jet in water, *J. Fluid Mech.* **878**, 98 (2019).
- [42] D. W. Murphy, X. Xue, K. Sampath, and J. Katz, Crude oil jets in crossflow: Effects of dispersant concentration on plume behavior, *J. Geophys. Res.: Oceans* **121**, 4264 (2016).
- [43] S. M. Masutani and E. E. Adams, Experimental study of multi-phase plumes with application to deep ocean oil spills, Final Report to U.S. Department of the Interior, Minerals Management Service, Contract No. 1435-01-98-CT-30964, 2000.
- [44] F. J. Diez, R. Sangras, G. M. Faeth, and O. C. Kwon, Self-preserving properties of unsteady round buoyant turbulent plumes and thermals in still fluids, *J. Heat Transfer* **125**, 821 (2003).
- [45] P. N. Papanicolaou and E. J. List, Investigations of round vertical turbulent buoyant jets, *J. Fluid Mech.* **195**, 341 (1988).

- [46] C. Brennen, *Fundamentals of Multiphase Flow* (Cambridge University Press, Cambridge, 2005).
- [47] G. I. Roth and J. Katz, Five techniques for increasing the speed and accuracy of PIV interrogation, *Meas. Sci. Technol.* **12**, 238 (2001).
- [48] J. Westerweel and F. Scarano, Universal outlier detection for PIV data, *Exp. Fluids* **39**, 1096 (2005).
- [49] M. Raffel, C. E. Willert, F. Scarano, C. J. Kähler, S. T. Wereley, and J. Kompenhans, *Particle Image Velocimetry: A Practical Guide* (Springer, Berlin, 2018).
- [50] J. Zhou, R. J. Adrian, S. Balachandar, and T. M. Kendall, Mechanisms for generating coherent packets of hairpin vortices, *J. Fluid Mech.* **387**, 353 (1999).
- [51] R. J. Adrian, C. D. Meinhart, and C. D. Tomkins, Vortex organization in the outer region of the turbulent boundary layer, *J. Fluid Mech.* **422**, 1 (2000).
- [52] C. C. K. Lai and S. A. Socolofsky, Budgets of turbulent kinetic energy, Reynolds stresses, and dissipation in a turbulent round jet discharged into a stagnant ambient, *Environ. Fluid Mech.* **19**, 349 (2019).
- [53] V. Todde, P. G. Spazzini, and M. Sandberg, Experimental analysis of low-Reynolds number free jets: Evolution along the jet centerline and Reynolds number effects, *Exp. Fluids* **47**, 279 (2009).
- [54] N. R. Panchapakesan and J. L. Lumley, Turbulence measurements in axisymmetric jets of air and helium. Part 2. Helium jet, *J. Fluid Mech.* **246**, 225 (1993).
- [55] H. C. Burridge, D. A. Parker, E. S. Kruger, J. L. Partridge, and P. F. Linden, Conditional sampling of a high Péclet number turbulent plume and the implications for entrainment, *J. Fluid Mech.* **823**, 26 (2017).
- [56] T. Djeridane, M. Amielh, F. Anselmet, and L. Fulachier, Velocity turbulence properties in the near-field region of axisymmetric variable density jets, *Phys. Fluids* **8**, 1614 (1996).
- [57] S. Gopalan and J. Katz, Flow structure and modeling issues in the closure region of attached cavitation, *Phys. Fluids* **12**, 895 (2000).
- [58] D. A. Drew and R. T. J. Lahey, Analytical modeling of multiphase flow, in *Particulate Two-Phase Flow*, edited by M. C. Roco (Butterworth-Heinemann, Oxford, 1993), pp. 509–566.
- [59] S. H. Hassan, T. Guo, and P. P. Vlachos, Flow field evolution and entrainment in a free surface plunging jet, *Phys. Rev. Fluids* **4**, 104603 (2019).
- [60] P. D. Friedman and J. Katz, Mean rise rate of droplets in isotropic turbulence, *Phys. Fluids* **14**, 3059 (2002).
- [61] B. Gopalan, E. Malkiel, and J. Katz, Experimental investigation of turbulent diffusion of slightly buoyant droplets in locally isotropic turbulence, *Phys. Fluids* **20**, 095102 (2008).
- [62] C. B. Da Silva, J. C. R. Hunt, I. Eames, and J. Westerweel, Interfacial layers between regions of different turbulence intensity, *Annu. Rev. Fluid Mech.* **46**, 567 (2014).
- [63] C. B. Da Silva, R. R. Taveira, and G. Borrell, Characteristics of the turbulent/nonturbulent interface in boundary layers, jets and shear-free turbulence, *J. Phys.: Conf. Ser.* **506**, 012015 (2014).
- [64] R. R. Taveira, J. S. Diogo, D. C. Lopes, and C. B. da Silva, Lagrangian statistics across the turbulent-nonturbulent interface in a turbulent plane Jet, *Phys. Rev. E* **88**, 043001 (2013).
- [65] X. Xue, L. D. Chandrala, and J. Katz, Dataset for “Flow structure and turbulence in the near field of an immiscible buoyant oil jet”, doi: [10.7266/Z7CJSDGF](https://doi.org/10.7266/Z7CJSDGF), Gulf of Mexico Research Initiative Information and Data Cooperative (GRIIDC), 2020, <https://Data.Gulfresearchinitiative.org>.